Ionization-induced proton and energy transfer in liquid water

Ludger Inhester ✉ 🆔 ; Arturo Sopena Moros 🆔 ; Sam Macé 🆔 ; Caroline Arnold 🆔 ; Robin Santra 🆔

Check for updates

View Online

Export Citation

Articles You May Be Interested In

Relaxation of the $2a_1$ ionized water dimer: An interplay of intermolecular Coulombic decay (ICD) and proton transfer processes

J. Chem. Phys. (June 2024)

AIP Publishing
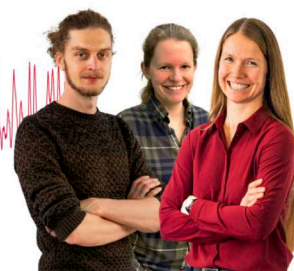
Ionization-induced proton and energy transfer in liquid water

Ludger Inhester,[1,2,a] (iD) Arturo Sopena Moros,[1] (iD) Sam Macé,[1,3] (iD) Caroline Arnold,[1,2,b] (iD)
and Robin Santra[1,2,4] (iD)

AFFILIATIONS

[1] Center for Free-Electron Laser Science CFEL, Deutsches Elektronen-Synchrotron DESY, Notkestr. 85, 22607 Hamburg, Germany
[2] The Hamburg Centre for Ultrafast Imaging, Luruper Chaussee 149, 22761 Hamburg, Germany
[3] École normale supérieure Paris-Saclay, Université Paris-Saclay, 94235 Cachan cedex, France
[4] Department of Physics, University of Hamburg, Notkestr. 9-11, 22607 Hamburg, Germany

[a] Author to whom correspondence should be addressed: ludger.inhester@cfel.de
[b] Current address: Helmholtz-Zentrum Hereon, Max-Planck-Straße 1, 21502 Geesthacht, Germany.

ABSTRACT

We report computational simulation results addressing the ionization response of liquid water upon valence ionization. The simulations cover ionizations in the whole valence-orbital range of liquid water, i.e., vacancies in $1b_1$, $3a_1$, $1b_2$, and $2a_1$ orbitals. It is found that ionization in any of these valence orbitals leads to rapid proton-transfer dynamics. The timescale on which the proton transfer occurs depends on which type of orbital is ionized. For ionization in the $2a_1$ orbitals, the proton transfer takes place in about 22 fs, competing with the intermolecular Coulombic decay mechanism that takes place on a similar timescale. This result is discussed in the context of earlier experimental results (Richter *et al.*, Nat. Commun. **9**, 4988) regarding the intermolecular Coulombic decay in water. For ionization in the outer-valence orbitals ($1b_1$, $3a_1$, $1b_2$), we see rapid internal conversion via non-adiabatic transitions to the electronic ground state. The proton transfer occurs 46, 70, and 91 fs after the initial ionization from a $1b_1$, $3a_1$, and $1b_2$ orbital, respectively. The initial valence ionization induces strong vibrational excitations in the surrounding water molecules, leading to a considerable increase in the local effective temperature. The created heat diffuses into the liquid environment on a timescale of several hundred femtoseconds. We compare the results using two different embedding schemes, subtractive and electrostatic embedding, and find overall very similar dynamics.

I. INTRODUCTION

Owing to its essential role in chemistry and biology, the dynamics of water triggered by ionizing radiation are of fundamental importance. Research fields, where radiation chemistry in water plays a crucial role, are radiation damage in living tissues,[1] oncology treatment,[2] or nuclear waste disposal.[3] In these contexts, the response of water triggered by *high-energy* radiation is particularly relevant, i.e., where the initially deposited energy is considerably larger than the ionization potential of water, which is 11.67 eV.[4] In liquid water, such radiation leads to the release of fast photoelectrons that induce further, secondary ionization. Eventually, electronic vacancies in all electronic levels are created, triggering relaxation processes and chemical dynamics through which ions and radicals in liquid water are created that then induce radiation damage in biological tissue or lead to corrosion.[3]

The most strongly bound orbitals, the core orbitals, have an ionization potential of about 540 eV.[5] The dynamics upon ionization from these orbitals mostly involve non-radiative electronic relaxation via Auger–Meitner decay accompanied by ultrafast proton transfer dynamics.[6–8] If the incident radiation has sufficient energy, the initial ionization process may be dominated by core ionization (depending on the specific type of radiation and the respective cross sections). Taking into account, however, all secondary ionization processes, ionization of electrons from valence orbitals is, in general, more abundant, because of their larger number, and because for each

primary ionization event, the released photoelectrons cause further ionization events. Even if the created photoelectrons initially have kinetic energies above the core-ionization threshold, through interacting with the water, they become slower and slower so that their kinetic energy falls at some point below the core-ionization threshold and, eventually, only valence ionizations remain energetically possible.

Valence ionization in liquid water generally implies an initial partially delocalized electron hole that quickly becomes localized on a single water molecule.[9] The ionization triggers reactions affecting the neighboring chemical environment, i.e., water molecules in the vicinity. The chain of the reaction starts with the transfer of a proton, in which the ionized water molecule donates one of its protons to a neighboring water molecule.[3] This fundamental reaction creates the hydroxide (OH) radical and the solvated proton, also often considered a hydronium cation (H_3O^+). Recently, this reaction has been tracked experimentally,[10] and via time-resolved x-ray absorption spectroscopy supported by corresponding computer simulations, the timescale of this reaction was found to be about 50 fs. In the experiment, however, the reaction was tracked only for holes in the $1b_1$ band, which were created through ionization via multi-photon absorption using an 800 nm laser. If one considers high-energy radiation, i.e., energies of the incident radiation of several hundred electron volts and higher, the relevant ionized electronic states are in general much more highly excited. The potential of tracking the ultrafast ionization-induced dynamics triggered by a pump pulse with high-energy radiation has recently been demonstrated using all-x-ray attosecond transient absorption spectroscopy (AX-ATAS).[11]

To address this regime, we focus in this work on computationally modeling the dynamics of water triggered by the removal of an electron from any valence orbital. In particular, we cover the whole range of valence orbitals, i.e., we address valence holes in the inner-valence orbitals ($2a_1$) as well as in the outer-valence orbitals ($1b_2$, $3a_1$, $1b_1$) of liquid water.

Whereas a number of research studies[9,10,12–14] focused on the ionization of liquid water from $1b_1$ orbitals, the dynamics triggered by the ionization to more highly excited outer-valence-ionized states ($1b_2^{-1}$, $3a_1^{-1}$) in liquid water have, to our knowledge, so far only been addressed for the water dimer.[15,16] Calculations indicate that ionization from $1b_1$ and $3a_1$ orbitals in the dimer leads to proton-transfer dynamics, regardless of whether the charge becomes localized on the hydrogen-bond donor or the acceptor unit (albeit involving a different timescale).[15] In contrast, ionization of the water dimer in one of the $1b_2$ orbitals was found to lead to dissociation into more complex ions and radicals such as OH, H, and H_2O^+.[15]

It is important to note that results on the dimer cannot be directly transferred to the liquid phase, since the liquid environment frustrates dissociation through caging. Furthermore, in a liquid environment, more possible reaction partners for a proton-transfer reaction are available than in a dimer, suggesting that proton-transfer reactions are more abundant than for the dimer. Moreover, the environment influences the reaction by transporting away excessive vibrational energy that, in a dimer, remains concentrated on the two molecules. Thus, relevant questions remain for the reaction dynamics triggered by high-energy radiation in liquid water.

Because of the fact that outer-valence orbitals $1b_2$, $3a_1$, and $1b_1$ have a similar binding energy, and given the fact that already in the water dimer, rapid internal conversion takes place,[15] it can be anticipated that an outer-valence hole rapidly relaxes to the ionized ground state via non-adiabatic coupling of the respective electronic states. Because of this presumably rapid electronic relaxation, ionizations in these orbitals can, on the one hand, be expected to lead to similar dynamics as if the ionization occurred from a $1b_1$ orbital. On the other hand, since the initial electronic-excitation energy is eventually transferred into vibrational degrees of freedom, the amount of vibrational energy for initial ionization from one of the deeper bound valence orbitals can be considerably larger than for initial ionization from a $1b_1$ orbital, thereby possibly affecting the resulting dynamics.

In contrast to vacancies in the outer-valence orbitals, the fate of inner-valence holes in liquid water involves a fundamentally different process: Intermolecular auto-ionization processes become energetically accessible. Through electron–electron interactions, an initial inner-valence ionized water molecule may decay into an energetically lower-lying ionized state, while the excess energy is used to ionize a neighboring water molecule. It was discussed that this autoionization process termed intermolecular Coulombic decay (ICD)[17–22] plays a major role for the relaxation of inner-valence-hole vacancies in liquid water and the subsequent radiation damage processes,[9,23–27] because it represents an efficient source of low-energy electrons, which are particularly harmful to bio-organic matter.[21] The rate for ICD for $2a_1$ vacancies in liquid water was estimated to be 12–52 fs.[28] At the same time, it was speculated that a water molecule with an inner-valence vacancy in liquid water is subject to rapid chemical dynamics involving a very fast proton transfer.[28] As the proton-transfer reaction progresses, the decay channel for ICD closes and, for the isolated water dimer, it was considered that proton transfer might even outpace ICD if the $2a_1$ vacancy is initially located on the hydrogen-bond donor unit.[27,28] Recent measurements of photoelectrons and ICD electrons detected in coincidence revealed that the efficiency for ICD in water clusters with hundreds of water molecules is about 40%–50%,[28] indicating that there is, indeed, a close competition between proton transfer and ICD.

To clarify the few-femtosecond dynamics in liquid water triggered by high-energy radiation, we report here results from mixed quantum–classical simulations performed with the fewest-switches surface hopping (FSSH) method. The liquid environment is described using quantum mechanics/molecular mechanics (QM/MM) embedding strategies.[29] We report on how the timescale of the non-adiabatic electronic relaxation and the proton-transfer reactions varies for the different initial ionization levels considering electronic vacancies in all valence orbitals. For a vacancy in the inner-shell $2a_1$ orbital, our calculations confirm the close competition between ICD and proton transfer. Moreover, we inspect how fast the liquid environment absorbs the vibrational energy injected into liquid water through the ionization process.

In Sec. II, we describe the simulation methodology, and in Sec. III, we present the simulation results. In Sec. IV, we draw final conclusions.

II. METHODS

The calculations are based on similar methods as those used in Ref. 10, but here, the range of initial valence vacancies considered is extended to cover the full range of valence orbitals. Moreover, we extend the embedding scheme and employ a somewhat larger basis set for the electronic-structure calculations as detailed below.

To generate geometric structures and momenta of water, we performed molecular dynamics (MD) simulations using GROMACS (version 2024.0)[30] using the SPC/E water force field.[31] To sample different configurations, an equilibrated box of 2652 water molecules was propagated for 100 ps using a time step of 2 fs at a temperature of 300 K and a pressure of 1 bar using periodic boundary conditions. For the MD calculations, we employed the particle-mesh-Ewald method (r_{cutoff} = 1 nm and a Fourier spacing of 0.16 nm), Parrinello–Rahman pressure coupling (τ_p = 2 ps), and velocity-rescale temperature coupling (τ = 0.1 ps).[32]

Starting from water structures sampled in these MD simulations, we further propagated the dynamics using the QM/MM method for 1 ps employing a time step of 0.5 fs. The QM/MM calculations were computed using GROMACS (version 4.5.5)[33] and XMOLECULE (version 0.2-465).[34,35] In these simulations, a randomly chosen cluster of 12 water molecules (the QM region) was described using the Hartree–Fock method and the 6-31+G basis set,[36,37] whereas the remaining water molecules (the MM region) were modeled using the force field employing the ONIOM embedding scheme.[38] In total, 100 different choices for the QM region were taken, leading to 100 different equilibrated QM/MM trajectories.

From these equilibration runs, a set of FSSH trajectories were performed starting after the removal of an electron from one of the valence orbitals. The FSSH trajectories were propagated for a total simulation time of 200 fs using a time step of 0.5 fs. We employed QM/MM embedding without periodic boundary conditions, the QM region was the same as for the respective equilibration runs, and the MM region incorporated all water molecules within a distance of 10.6 Å with respect to the center of the QM region. For each final snapshot of the 100 QM/MM-equilibration trajectories, we initiated three FSSH trajectories; in each of them, a valence orbital for the initial electronic vacancy was randomly chosen. The FSSH trajectories were computed using the chemical dynamics toolkit (CDTK)[39] with gradients and non-adiabatic couplings calculated on the fly using XMOLECULE. Non-adiabatic couplings were incorporated via calculated coupling vectors; for hopping events, we employed rescaling of the velocities in the direction of the coupling vectors. Within XMOLECULE, Gaussian-basis-set integrals were evaluated using the libcint library (version 6.1.2).[40]

The electronic-structure model used for the various ionized states is based on Koopmans' theorem. In this approach, we compute the neutral Hartree–Fock state and describe the potential energy, its gradient, and the non-adiabatic coupling vectors of the ith ionized state based on the assumption that the corresponding energy is given by $E_i = E - \varepsilon_i$, where E is the neutral Hartree–Fock energy and ε_i is the restricted-Hartree-Fock orbital energy associated with orbital i. This electronic-structure model is a computationally efficient and reliable method to obtain all the singly ionized electronic states. It turned out to give qualitatively correct surfaces in similar contexts.[10,41–44] We note, however, that this approximation has to be considered with care, specifically when higher excited states, i.e., those with vacancies in deeper bound valence orbitals such as $2a_1$, are considered, because the relaxation effects of the electronic structure upon removal of an electron are entirely missing. We have, therefore, tested our approach by scanning potential energy surfaces for the water dimer geometry. Figure 1 shows a scan along the proton transfer coordinate for a water dimer when an electron is removed from the $2a_1$ orbital on the hydrogen-donating water molecule. The scan obtained using Koopmans' theorem is compared to the one obtained using the restricted open-shell Hartree–Fock (ROHF) method, in which we optimized the electronic structure self-consistently in the presence of the inner-valence hole. Convergence to the desired inner-valence-hole state was achieved using the maximum-overlap method.[45,46] Moreover, we compare with the potential-energy-surface scan extracted from Ref. 28 based on multi-state state-averaged complete-active-space self-consistent-field calculations with second-order perturbative corrections (MS-CASPT2) and a somewhat larger basis set (6-31++G**). As can be seen, with all three methods, qualitatively similar potential energy curves are obtained, confirming that Koopmans' theorem approximation for the $2a_1$-vacancy states is valid. Given the fact that, in liquid-water simulations, we do not find any considerable specificity with respect to the individual $2a_1$ orbital that is ionized, we think that this electronic-structure model is adequate to qualitatively address the immediate response of water to ionizing radiation.

We employed two different embedding schemes for the FSSH calculations. In the first one, the ONIOM subtractive scheme is employed.[38] Within this embedding scheme, the potential energy
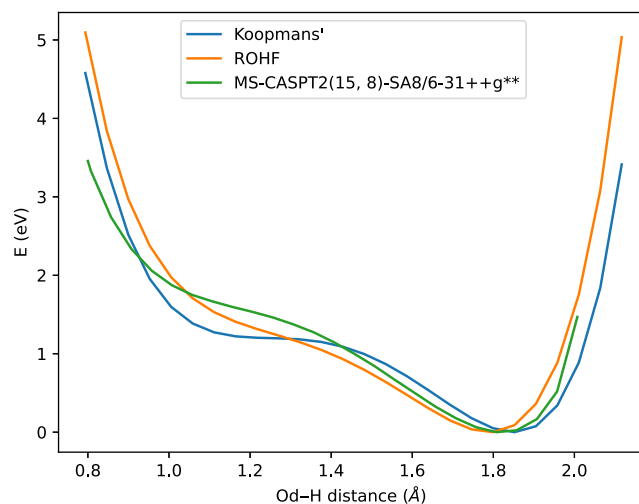

FIG. 1. Scan of the potential energy surface along the oxygen-donor–hydrogen coordinate for $2a_1$-valence hole states for the water dimer. The electron vacancy is placed on the hydrogen-bond-donor molecule. Compared are three different electronic-structure methods: Koopmans' theorem/6-31+G, ROHF/6-31+G, and MS-CASPT2(15, 8)-SA8/6-31++g** (extracted from Ref. 28).

is computed as a function of atomic positions $\mathbf{r}$ in a subtractive manner as

$$E(\mathbf{r}_{\text{total}}) = E_{\text{MM}}(\mathbf{r}_{\text{total}}) + E_{\text{QM}}(\mathbf{r}_{\text{QM region}}) - E_{\text{MM}}(\mathbf{r}_{\text{QM region}}), \quad (1)$$

where $E_{\text{MM}}(\mathbf{r}_{\text{total}})$ is the potential energy evaluated from the force field for all molecules (MM region and QM region), $E_{\text{MM}}(\mathbf{r}_{\text{QM region}})$ is the potential energy evaluated from the force field for the molecules in the QM region, and $E_{\text{QM}}(\mathbf{r}_{\text{QM region}})$ is the energy obtained from electronic structure calculations involving the molecules in the QM region. It is important to note that the electronic-structure calculations do not take into account the MM environment. Thus, electrons see the effect of the surrounding water molecules only implicitly via the MM forces that are applied to the respective atoms in the QM region. Moreover, interaction between the MM and QM regions is purely covered on the level of the force field, i.e., the QM and MM molecules interact via the partial charges and Lennard-Jones potentials as specified in the force-field parameters. This implies that the MM region is only indirectly affected by the ionization in the QM region.

The other embedding scheme follows the idea of electrostatic embedding. In particular, the potential energy is computed in an additive manner as

$$E(\mathbf{r}_{\text{total}}) = E_{\text{QM}}(\mathbf{r}_{\text{QM region}}, \mathbf{r}_{\text{MM region}})$$
$$+ E_{\text{LJ}}(\mathbf{r}_{\text{QM region}}, \mathbf{r}_{\text{MM region}}) + E_{\text{MM}}(\mathbf{r}_{\text{MM region}}), \quad (2)$$

where the energy $E_{\text{MM}}(\mathbf{r}_{\text{MM region}})$ is the force-field energy evaluated only for the molecules in the MM region, i.e., it only covers MM-region–internal interactions. Additional Lennard-Jones (LJ) interaction between the QM region and the MM region $E_{\text{LJ}}(\mathbf{r}_{\text{QM region}}, \mathbf{r}_{\text{MM region}})$ is added in Eq. (2). The same parameters for the LJ interaction terms are employed as specified in the SPC/E force field. In Eq. (2), the term $E_{\text{QM}}(\mathbf{r}_{\text{QM region}}, \mathbf{r}_{\text{MM region}})$ is the energy obtained from the quantum-mechanical electronic-structure calculation that incorporates all atoms of the MM region in the calculation as smeared-out charges. By including these smeared-out charges in the electronic-structure calculation, the electrostatic embedding scheme incorporates electrostatic interaction between the nuclei and the electrons in the QM region and the charge distribution of the surrounding MM region. In particular, each MM atom is represented by the respective charge as defined in the SPC/E force field, and its charge density is modeled via Gaussian functions with a standard deviation given by the respective covalent radius of the atom (0.66 Å for oxygen and 0.31 Å for hydrogen[47]). The usage of Gaussian-type charges with the overall fractional value was made possible via a modification of the libcint library. Smeared-out Gaussian-type charge distributions were employed before to avoid over-polarization of the QM region.[29] In our simulations, we observe that employing smeared-out atomic charge distributions overcomes numerical instabilities when one of the hydrogen atoms of the QM region comes close to one of the MM atoms.

Computing the gradients and non-adiabatic couplings for Koopmans' theorem states requires solving the coupled-perturbed Hartree–Fock (CPHF) equations.[48,49] When using electrostatic embedding, solving the CPHF equations for all the coordinates (including all the MM atoms) can be prohibitively computationally

expensive, because the implicit effects on the electronic structure for all the atom positions (QM and MM regions) have to be solved in the CPHF equations self-consistently. To overcome this problem, we simplify the CPHF equations by treating the MM atoms using the uncoupled approximation as described in Ref. 50. In the resulting FSSH trajectories, we observe a total-energy drift of 0.2 eV (median of the absolute energy change after 200 fs simulation time). In order to test the convergence of the calculations with respect to the size of the QM region, we also performed calculations with a smaller QM region (see Appendix B).

III. RESULTS

In the following, we focus on discussing results obtained with the electrostatic embedding scheme. Results for the ONIOM embedding scheme are given in Appendix A and are only discussed when we find noticeable differences.

A. Electronic relaxation

The density of valence-hole states in liquid water is visualized by the histogram of electron-binding energies in Fig. 2. In the histogram, we group the valence orbitals employing the symmetry nomenclature for an isolated water molecule, i.e., we employ the usual labels $1b_1$, $3a_1$, $1b_2$, and $2a_1$. The labeling is done according to the relative energy position in the electronic structure of the QM region considering that it contains 12 water molecules, i.e., the highest occupied molecular orbital (HOMO) to HOMO-11 were assigned to $1b_1$, the orbitals HOMO-12 to HOMO-23 were assigned to $3a_1$, and so on. We note that in liquid water, orbitals are somewhat deformed due to structural fluctuations and exhibit some degree of mixing among different water molecules. Accordingly, the orbitals do not strictly follow the mentioned symmetry implied by the labels. This is even more the case when we follow a dynamical situation like a proton transfer reaction. However, for simplicity, we still refer to the orbitals using these symmetry labels.
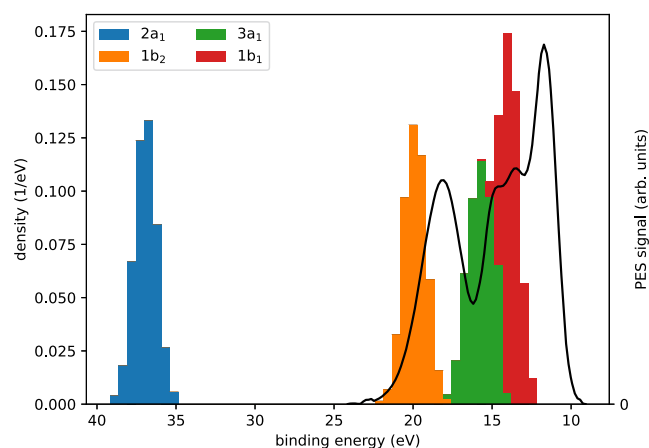

FIG. 2. Density of states obtained from the orbital energies of the sampled QM clusters. The black line shows the experimental photoelectron spectrum from Ref. 51 for a photon energy of 32.6 eV.
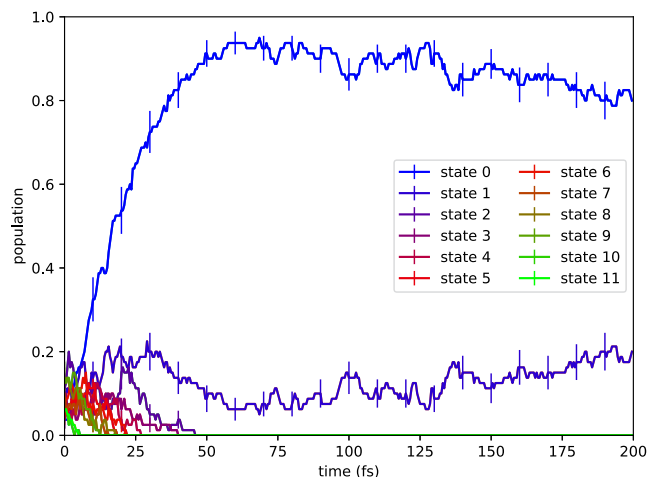
23 April 2025 08:13:16

FIG. 3. Active-state populations for the ensemble of trajectories starting with a $1b_1$ valence hole. The error bars indicate the standard error.

As one can see in Fig. 2, the two groups $1b_1$ and $3a_1$ energetically overlap; otherwise, the different valence levels are energetically largely distinct. In particular, there is a large gap between the inner-valence levels $(2a_1)$ and the outer-valence levels of more than 10 eV.

The density of states generated from the orbital energies is compared in Fig. 2 with the experimental photoelectron spectrum for a photon energy of 32.6 eV, which was extracted from Ref. 51. The shape of the calculated density of state is overall consistent with the one shown in the experimental spectrum. However, the experimental binding energies are lower by about 2 eV. This mismatch

must be attributed to orbital relaxation effects that are missing when evaluating the binding energies via Hartree–Fock orbital energies. More specifically, photoionization in bulk water leads to polarization of the electronic structure even beyond the QM cluster considered here. This effect, which is absent in our calculations, leads in general to lower binding energies.

As already anticipated, the high density of states in liquid water leads to rapid internal conversion through non-adiabatic transitions. An electron initially removed from one valence orbital is thus rapidly transferred to an electronic vacancy in another orbital, leading on average to the population of energetically lower-lying electronic states. In our simulation, this electronic decay is modeled in the FSSH trajectories by the change of the current active state of each trajectory. In Fig. 3, we show the fraction of trajectories in a specific active electronic state (0–11) for trajectories initiated with a hole in one of the $1b_1$ valence orbitals. Due to the random initialization, each state is initially almost equally populated. The electronic state quickly relaxes to the ground state (state 0) and the lowest excited state (state 1).

Figure 4 shows the fraction of trajectories having an active state with a valence hole in one of the above-introduced orbital groups. The hole populations are shown for trajectories starting with a valence hole in one of the $1b_1$ [Fig. 4(a)], $3a_1$ [Fig. 4(b)], $1b_2$ [Fig. 4(c)], and $2a_1$ [Fig. 4(d)] orbitals, respectively. As one can see, for an initial outer-valence vacancy in one of the $3a_1$ or $1b_2$ orbitals, the active-state population moves within a few femtoseconds to hole states with a vacancy in one of the $1b_1$ orbitals. The rapid electronic relaxation dynamics are further quantified by a fit of the time-dependent populations. The dashed lines show fits assuming a sequential decay process $(1b_2^{-1} \rightarrow 3a_1^{-1} \rightarrow 1b_1^{-1})$. While trajectories starting with a hole in the $1b_1$ orbital almost exclusively stay in a hole configuration within that group [Fig. 4(a)], it takes about 20 fs for a $3a_1$ valence hole to turn into a $1b_1$ valence hole [Fig. 4(b)]. For
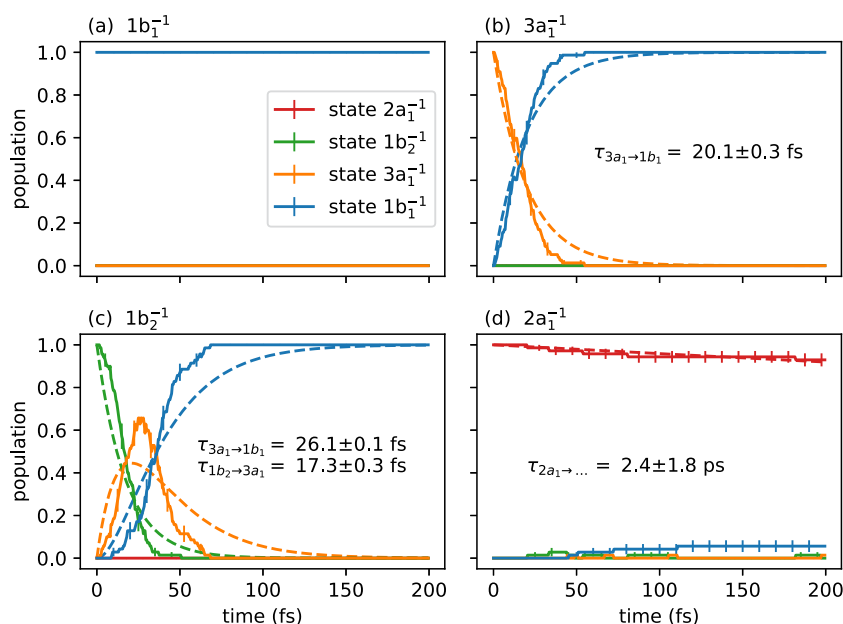

FIG. 4. Active-state populations for trajectories starting with an initial valence hole in $1b_1$ (a), $3a_1$ (b), $1b_2$ (c), and $2a_1$ (d), using electrostatic embedding. The error bars indicate the standard error. The dashed lines show fits assuming a kinetic-rate-equation model for a sequential decay $1b_2^{-1} \rightarrow 3a_1^{-1} \rightarrow 1b_1^{-1}$. For $2a_1^{-1}$, only a single decay curve is fitted.

23 April 2025 08:13:16

trajectories starting with a deeper bound $1b_2$-valence hole, it takes a similar time (17 fs) to decay into an intermediate $3a_1$ hole configuration. The subsequent decay to a $1b_1$ hole configuration takes place in about 26 fs.

These electronic decay dynamics are substantially different from the scenario where the electronic vacancy is initially in a $2a_1$ orbital. Here, it takes about 2.4 ps for the electronic decay to occur. The electronic decay from these inner-valence levels is much slower due to the much larger energetic separation of the $2a_1$ orbital to the other ones (see Fig. 2), which suppresses non-adiabatic couplings between inner- and outer-valence-hole states.

B. Number of proton transfers

In all trajectories, we observe that a proton is transferred to a neighboring water molecule. In order to analyze the number of proton transfers, we associated each hydrogen with its closest oxygen atom. When a hydrogen atom moves toward another oxygen atom and, thus, this assignment changes, we consider a proton transfer to have happened. Figure 5 shows the average number of such proton-transfer reactions for trajectories starting in a respective initial hole configuration. The average number of proton transfers increases rapidly and reaches within the 200 fs simulation time, a value of about 1.5, indicating that on average more than one proton transfer occurs. Inspection of individual trajectories reveals that after a proton has been transferred, the water molecule that has accepted the initial proton can, after some time, give away a proton to a third water molecule. This reflects the highly dynamical character of the solvated proton, which migrates through the water via structural diffusion, a process known as Grotthuss mechanism.[52,53]

As can be seen, for an initial valence hole in one of the $1b_1$ orbitals [Fig. 5(a)], the proton-transfer reaction starts a bit earlier as compared to the case when the hole is initially in one of the $3a_1$ orbitals [Fig. 5(b)]. For a $1b_2$ valence hole, the proton transfer occurs even later [Fig. 5(c)]. In contrast, for a $2a_1$ hole state [Fig. 5(d)], it starts significantly earlier.

C. Proton-transfer coordinates

To further study the progress of the proton-transfer reaction, we identified the atoms involved in the first proton-transfer reaction, based on the same geometrical criterion as used before in Fig. 5.

In Fig. 6, we plot the average distances between proton and donor oxygen (Od–H), proton and acceptor oxygen (Oa–H), as well as the two involved oxygen atoms (Oa–Od). The analysis confirms the earlier observation: When the valence hole is initially placed in one of the $1b_1$ orbitals, the proton transfer occurs earlier than when the valence hole is initially in one of the deeper-bound $3a_1$ or $1b_2$ orbitals. For the $2a_1$ orbitals, however, the proton transfer occurs much earlier than for all the outer-valence orbitals. Overall, one can read out the time of the proton transfer as the time when, on average, the distance Od–H becomes larger than Oa–H, yielding 46 fs for an initial $1b_1$ valence hole, 70 fs for an initial $3a_1$ valence hole, 91 fs for an initial $1b_2$ valence hole, and 22 fs for an initial $2a_1$ valence hole.

One can also recognize in Fig. 6 that during the proton transfer, the participating oxygen atoms come closer to each other. After the proton transfer, the distance between these two oxygen atoms increases again. We compare this distance to the average oxygen–oxygen distance for water molecules within the first solvation shell evaluated for all water molecules in the QM region (red line in Fig. 6). This distance indicates that after the proton transfer has happened, the two participating molecules, i.e., the remaining OH and H_3O^+, move away from each other. This characteristic change of Od–Oa is responsible for transient energetic
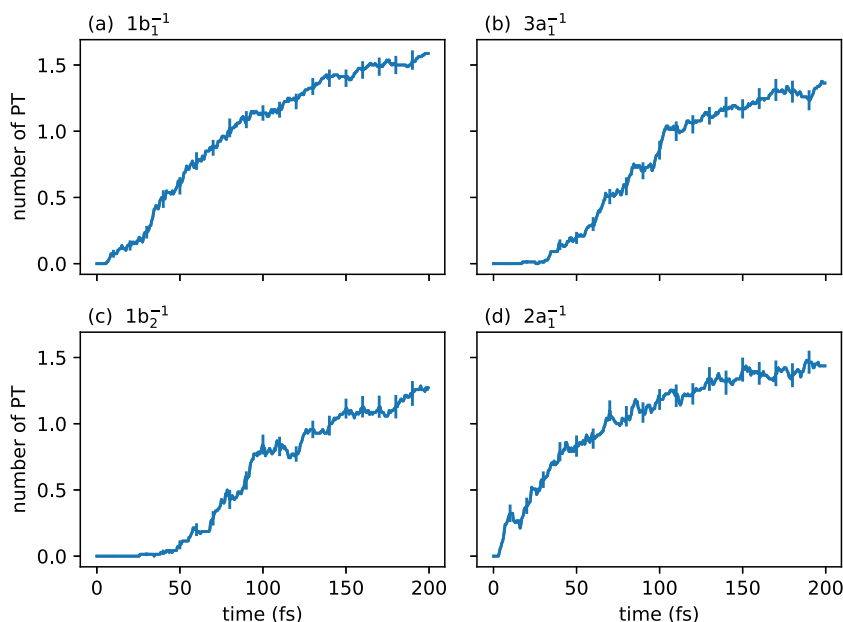

FIG. 5. Average number of proton transfers for trajectories starting with an initial valence hole in $1b_1^{-1}$ (a), $3a_1^{-1}$ (b), $1b_2^{-1}$ (c), and $2a_1^{-1}$ (d), using electrostatic embedding. The error bars indicate the standard error.
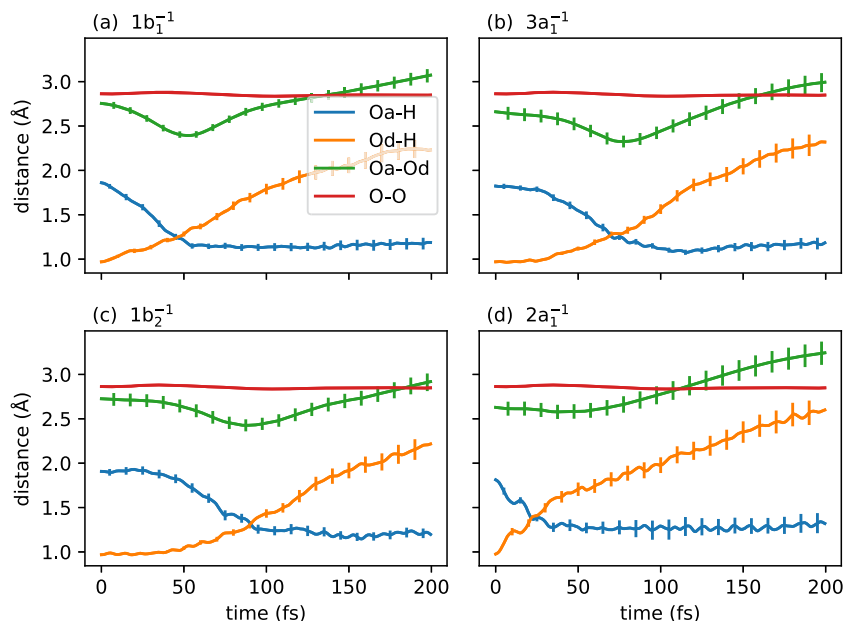
FIG. 6. Proton-transfer coordinates for trajectories starting with an initial valence hole in $1b_1$ (a), $3a_1$ (b), $1b_2$ (c), and $2a_1$ (d), using electrostatic embedding. The error bars indicate the standard error.

shifts in the spectroscopic transitions through which it was possible to track the proton-transfer reaction via time-resolved x-ray absorption measurements.[10]

The much faster proton-transfer dynamics for $2a_1$ valence holes are in qualitative agreement with recent simulations for the water dimer. Considering that the vacancy is placed on the proton-donating unit in a dimer, Richter et al.[28] report an even smaller timescale of 8 fs and Kumar et al.[27] give a timescale of 14 fs for the completion of the proton transfer. Note that the value of 22 fs taken from Fig. 6(d) describes the time at which the proton has a greater distance from the donor oxygen than from the acceptor oxygen. The quantitative difference led us to perform additional simulations for an ensemble of water dimers, where we also observed a shorter proton-transfer timescale than for the liquid (the distance Od–H becomes larger than Oa–H at 3.8 fs). Thus, the somewhat larger value for the liquid must be attributed to the larger structural heterogeneity in the liquid.

The $2a_1$ valence hole undergoes ICD decay if the proton transfer has not already progressed too far. Following Richter et al.,[28] we evaluated the fraction of trajectories where the ICD channel is still open using the criterion that the distance of any hydrogen atom to the oxygen atom in the proton-donating molecule remains below 1.3 Å. Figure 7 depicts the respective fraction of trajectories initiated with a $2a_1$ valence hole as a function of time. The exponential fit in the figure reveals a half-life time of $t_{open} = 18.9 \pm 1$ fs for the closing of the ICD channel in liquid water—a noticeably larger value than previously obtained by Richter et al.[28] for the dimer (2.9 fs).

We can map the effective ICD probability α to an ICD lifetime τ_{ICD} assuming a competition between proton transfer and ICD decay via[28]

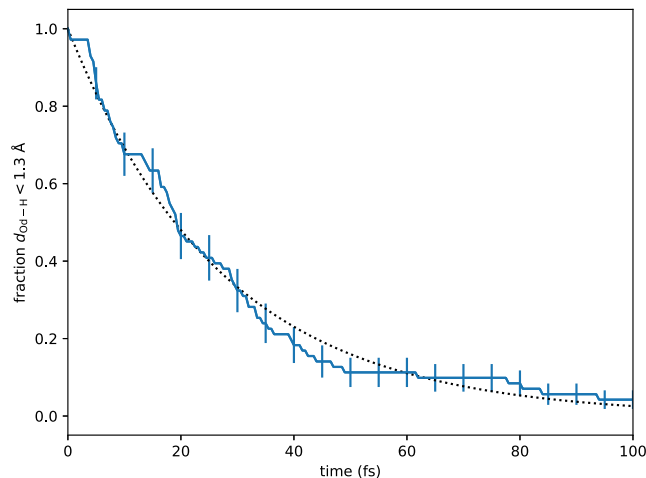$$\alpha = 1 - \exp\left(-t_{open}/\tau_{ICD}\right). \qquad (3)$$

FIG. 7. Fraction of trajectories for which the oxygen–hydrogen distances of the proton-donating water molecule remain below 1.3 Å. The error bars indicate the standard error. The dotted line shows an exponential fit.

In Ref. 28, ICD probabilities have been measured for water cluster of different sizes, revealing an ICD probability α that increases with cluster size. In particular, a value of $\alpha \simeq 0.5$ for water clusters with an average number of $\langle N \rangle = 250$ water molecules was measured, and the measurements suggested that the ICD probability α increases further with $\langle N \rangle$. Extrapolating this value toward bulk water, Table I lists ICD decay times τ_{ICD} evaluated via Eq. (3) for ICD probabilities $\alpha = 0.5$, 0.6, and 0.7, employing our value of t_{open} computed for bulk water and the earlier value of t_{open} computed for water dimers. As

23 April 2025 08:13:16

TABLE I. Calculated ICD decay times for bulk water for a given ICD probability α.

	τ_{ICD} in fs	
α	t_{open} = 18.9 ± 1 fs	t_{open} = 2.9 fs
0.5	27.3 ± 1.6	4.2
0.6	20.6 ± 1.2	3.2
0.7	15.7 ± 0.9	2.4

one can see, the larger value for t_{open} yields effective ICD probabilities that agree reasonably well with the value τ_{ICD} = 23 fs that has been extrapolated from the corresponding ICD decay rate calculations for the dimer.[28] Given that τ_{ICD} is larger than 10 fs, a value of t_{open} = 2.9 fs is incompatible with $\alpha > 0.5$. The measurements performed by Richter et al.[28] thus are consistent with the larger t_{open} we obtain for bulk water.

D. Local heating and cooling

The ionization places considerable vibrational excitation into the liquid water. As discussed in Fig. 4, the initial electronic state decays in a few tens of femtoseconds to the electronic ground state, unless the initial hole is in an inner-valence orbital. Considering an initial valence hole in a $1b_2$ orbital, the rapid relaxation to the electronic ground state with a hole in a $1b_1$ orbital implies an (electronic) relaxation energy of about 7 eV (see Fig. 2). However, even without this electronic decay, the ionization induces motion in various vibrational degrees of freedom, because potential energy surfaces in the ionized states are considerably different in shape compared to those in the neutral ground state.

Assuming that an energy of 7 eV is transferred to the vibrational degrees of freedom of a water molecule and the four molecules in its first solvation shell, each of these water molecules gains a vibrational energy of about 1.4 eV, implying significant vibrational excitation. In thermodynamic equilibrium, this would correspond to a temperature increase of about 1800 K for the involved five water molecules. Meanwhile, one must consider that the vibrational energy is quickly distributed into the farther chemical environment of the liquid water and, thus, it is quickly shared among many more water molecules.

To inspect this vibrational energy transfer, we compute from the simulation the effective temperature of water molecules following valence-electron removal. The effective temperature as a function of time is determined from the instantaneous average kinetic energy per atom $E_{kin,atom}$, via

$$T = 2 \, E_{kin,atom}/3 \, k_B. \tag{4}$$

To inspect how quickly the vibrational energy spreads over different spatial regions, we compute the effective temperature for groups of molecules at various distances from the created OH radical. In particular, we consider the atoms of the water molecule ending up in the created OH radical plus the five water molecules in the QM region closest to it (QM1), the remaining six water molecules in the QM region (QM2), the six closest water molecules in the MM region (MM1), and the next six closest water molecules in the MM region (MM2). Here, one has to consider that due to the bond-length

restrictions in the force field, kinetic energy cannot be put into internal vibrations of the MM molecules. Therefore, additional kinetic energy can only appear as rotational or translational energy of each water molecule, whereas for the QM region, the hydrogen–oxygen bond length and the bond angles move classically in the respective *ab initio* potential.

For an initial $1b_1$ valence hole, Fig. 8(a) shows how the effective temperature rapidly increases for the QM1 region. As a consequence of the sudden ionization, water molecules start to rearrange and thereby gain vibrational energy. At about t = 78 fs, the effective temperature reaches a maximum of about 798 K and starts to decline after that. The next closest water molecules (QM2 region) show a much smaller increase in temperature and remain at a temperature below 480 K. The corresponding temperatures of the MM1 and MM2 regions increase as well, approaching 460 and 430 K, respectively.

For the simulations with an initial $3a_1$ hole [Fig. 8(b)], a similarly rapid temperature increase can be observed. The amount of vibrational energy placed into the system is somewhat larger, leading to a stronger rise in the effective temperature, particularly for the QM regions. The temperature for the QM1 region grows up to 919 K at t = 100 fs and decreases afterward, whereas the one for the QM2 reaches a plateau of 582 K at t = 50 fs. The temperature for the MM regions goes as high as 477 and 433 K, respectively.

An even stronger increase in the effective temperature can be seen for an initial $1b_2$ hole [Fig. 8(c)]. Here, the temperature in the QM1 region reaches a maximum of 1268 K at about 94 fs. The maximum for the QM2 region is reached somewhat earlier (918 K at about 58 fs). A decline of the temperature in the QM1 and QM2 regions can be seen on an estimated timescale of several hundred femtoseconds. Similarly as for the other valence holes, the effective temperature of the MM regions steadily increases, reaching about 499 and 441 K, respectively.

Even though the inner-valence $2a_1$ orbitals have a much larger binding energy, which means that their ionization involves a much larger electronic excitation energy, the situation is different here, since the electronic relaxation happens much more slowly (see Fig. 4) so that within the simulation time, the electronic excitation energy almost exclusively remains in the electronic degrees of freedom. Accordingly, the increase in the effective temperature is not as large as one would expect from the electronic excitation energy. Meanwhile, the much more rapid proton transfer dynamics suggest that the potential energy surfaces around the equilibrium geometries are considerably steeper than for the outer-valence holes. From this consideration, one might expect a much stronger increase in the effective temperature than, for example, for an initial $1b_1$ hole. It turns out that the trends in the temperatures are similar to those for an initial $1b_2$ hole: Up to about 85 fs, the temperature in the QM1 region increases. It reaches a maximum of about 1188 K and then starts to decay. The temperature in the QM2 region grows noticeably more slowly and reaches a plateau with a value of 654 K at about 125 fs. The temperatures in the MM regions go as high as 502 and 426 K, respectively.

Overall, the analysis of the effective temperature shows that the ionization involves a considerable enhancement of vibrations in the liquid environment, which corresponds to a significant increase in the local temperature. The vibrational energy is distributed over the liquid environment within several hundred
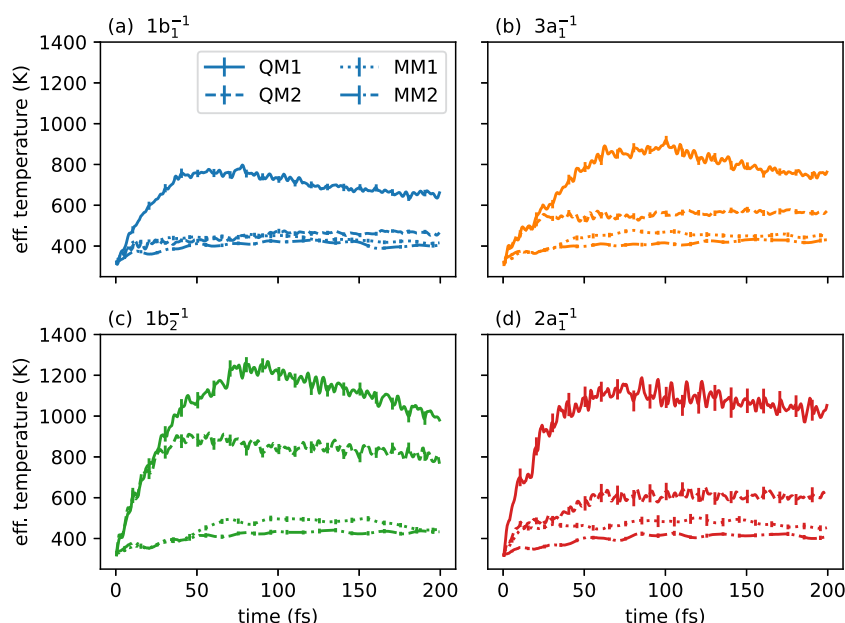
FIG. 8. Effective temperature evaluated for different sets of molecules: The atoms of the molecule ending up as OH radical plus the five closest molecules in the QM region next to it (QM1, solid line), the other six molecules in the QM region (QM2, dashed line), the six closest water molecules in the MM region (MM1, dotted line), and the next nearest six water molecules in the MM region (MM2, dotted-dashed line), for trajectories with an initial valence hole in (a) $1b_1$ (blue), (b) $3a_1$ (orange), (c) $1b_2$ (green), and (d) $2a_1$ (red), using electrostatic embedding.

femtoseconds. The increase in the local temperature remains spatially constrained in the sense that only the closest six molecules (i.e., approximately the first solvation shell) experience temperatures above 1000 K.

Figure 8 illustrates that photoionization provides a means to locally heat up water on very short timescales. For aqueous solutions, the very steep and transient increase in effective local temperature might trigger reactions involving solvated species in the vicinity of the radiolysis reaction. This effect can also be regarded as a tool to trigger chemical reactions, i.e., it opens up possibilities to investigate ultrafast chemical reactions in aqueous solutions that can then be tracked via pump–probe schemes. The method that is also known as the temperature-jump technique has been introduced using infrared laser radiation[54] and has been considered also with THz radiation.[55,56] Our results suggest that with temporally constrained high-energy radiation, considerable local temperature jumps of more than 1000 K may be reached as well.

The results for the electrostatic embedding (Fig. 8) are somewhat different compared to the results for the ONIOM embedding, which are shown in Fig. 9. Overall, one can see that the effective temperature of the QM regions reaches noticeably higher values with the ONIOM embedding than with the electrostatic embedding. Correspondingly, the temperatures of the MM regions remain lower. This demonstrates a somewhat more rapid heat transfer from the QM region into the MM region for electrostatic embedding compared to the one for the ONIOM embedding. The discrepancy must be attributed to the less direct coupling of the MM molecules to the QM region in the latter. In fact, since, for the former, forces calculated for the MM molecules involve the actual electronic structure of the QM region, the effect of the overall positive electric charge can be seen by the MM molecules directly. For the ONIOM embedding, in contrast, MM molecules effectively

interact with a neutral QM region, leading to a much more indirect coupling.

E. Localization of the proton transfer

Conceptually, embedding schemes introduce artificial layers into the simulation by splitting up the system into a QM region and an MM region, whereas in reality, the bulk-water system is homogeneous. To identify possible artifacts from this QM/MM separation, we inspect the positions of the created radicals and of the excess proton in the simulation. In particular, we inspect their distances from the center of mass of the molecules that are part of the QM region (COM). It is insightful to understand where in the QM region the proton transfer occurs and whether the QM/MM interfacial region plays a distinct role in the simulations. In Fig. 10, the average distances of various species from the COM are shown. In particular, the figure shows the distance of oxygen and hydrogen atoms (both averaged over the molecules in the QM region), as well as the distance of the oxygen atom belonging to the formed OH radical and the distance of the excess proton from the COM. In order to determine the position of the excess proton, we employ the excess-proton-analysis framework introduced in Ref. 57. In particular, we compute the position of the excess proton as

$$\mathbf{r}_p = \left(\sum_i^{N_O} \mathbf{r}_i w_i\right) \Big/ \left(\sum_i w_i\right), \tag{5}$$

with

$$w_i = \sum_j^{N_H} \left\{ 1 + \exp\left[\left(d_{ji} - \hat{d}\right)/\eta\right] \right\}^{-1}, \tag{6}$$

where $\hat{d} = 1.4$ Å, $\eta = 0.05$ Å, the sum in Eq. (5) runs over all oxygen atoms, the sum in Eq. (6) runs over all hydrogen atoms, and d_{ji} is the
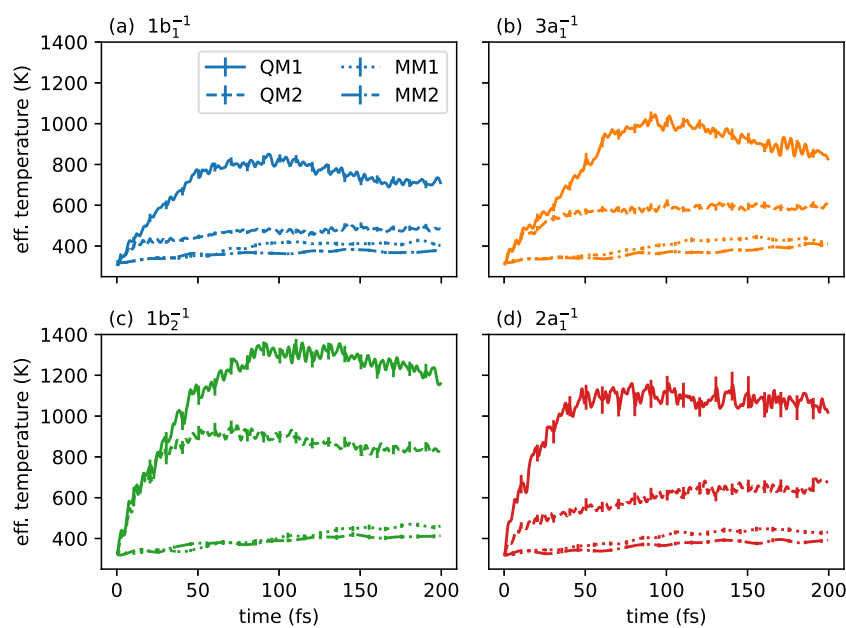
FIG. 9. Effective temperature evaluated for different sets of molecules: The atoms of the molecule ending up as OH radical plus the five closest molecules in the QM region next to it (QM1, solid line), the other six molecules in the QM region (QM2, dashed line), the six closest water molecules in the MM region (MM1, dotted line), and the next nearest six water molecules in the MM region (MM2, dotted-dashed line) for trajectories with an initial valence hole in (a) $1b_1$ (blue), (b) $3a_1$ (orange), (c) $1b_2$ (green), and (d) $2a_1$ (red), using ONIOM embedding.
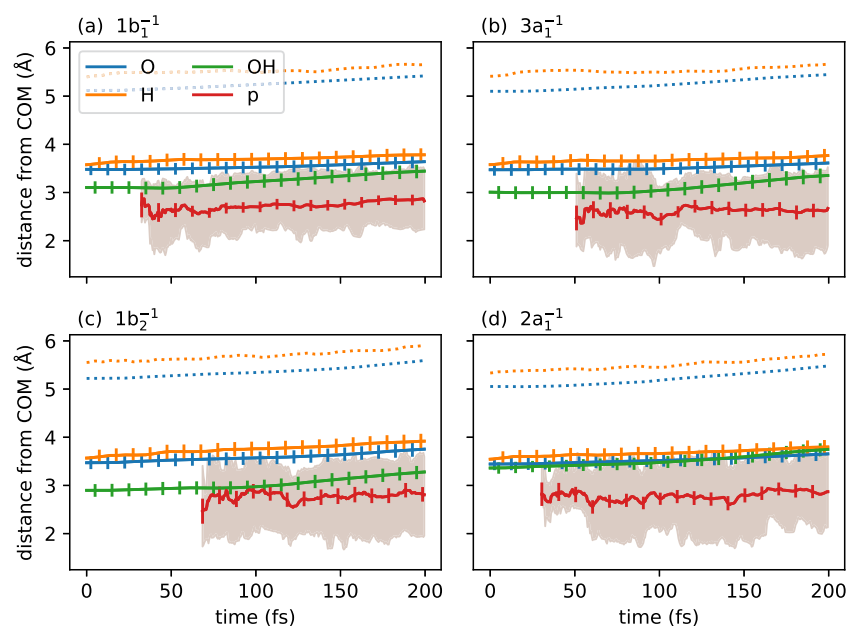

FIG. 10. Distances of QM atoms from the center of mass of the QM region as a function of time for trajectories starting with an initial valence hole in $1b_1$ (a), $3a_1$ (b), $1b_2$ (c), and $2a_1$ (d), using electrostatic embedding. Average distance of the oxygen atoms (O, blue), average distance of the hydrogen atoms (H, orange), distance of the oxygen involved in the formation of the OH radical (OH, green), and distance of the excess proton (p, red). The error bars depict the standard error. The shaded red areas depict the standard deviation for the proton. The dotted lines show the maximum oxygen (blue) and hydrogen (orange) distances in the QM region.

distance between the ith oxygen atom and the jth hydrogen atom. In contrast to the analysis performed in Fig. 6, this tracks the position of the excess proton not as an individual atom, but as a structural property. Thus, it allows one to follow the position of the excess proton even beyond several proton transfer reactions.

As one can see in Fig. 10, for all three outer-valence holes, the oxygen atom that is part of the later formed OH is, on average, somewhat closer to the COM than the average oxygen atom in the QM region (O). The same holds for the excess proton (p), which is closer to the COM than the average hydrogen atom in the QM region (H).

These features result from some selectivity of the proton transfer reaction: By construction, the valence hole is constrained to the QM region and the embedding scheme effectively prohibits proton transfer from water molecules in the QM region toward oxygen atoms in the MM region. Accordingly, proton transfer occurs only within the QM region. The resulting bias (which is to some degree inherent to QM/MM simulations) leads to the creation of OH and an excess proton in the inner part of the QM region. Thus, the distance of the OH radical from the COM is smaller than the distance of O from the COM. The same trend is observed even more pronounced for
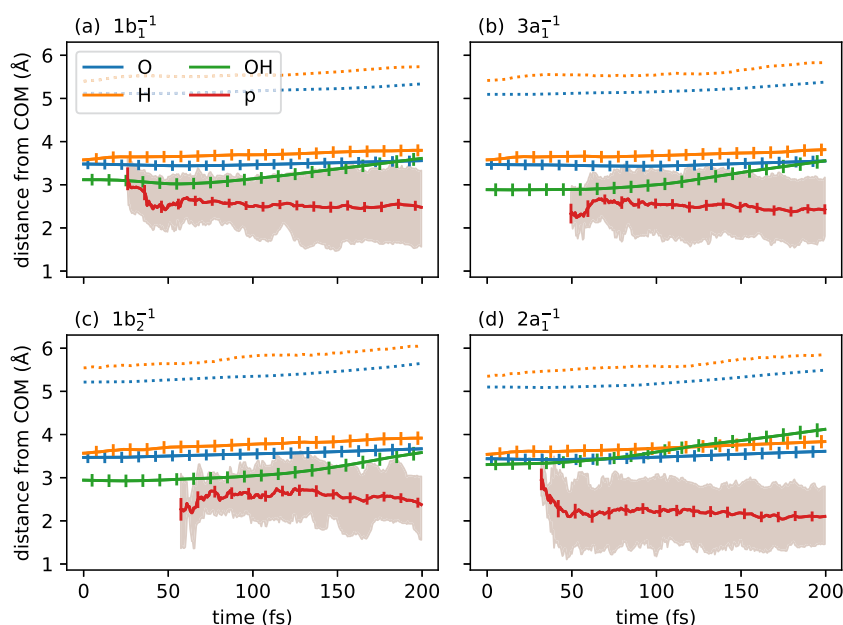
FIG. 11. Distances of QM atoms from the center of mass of the QM region as a function of time for trajectories starting with an initial valence hole in $1b_1$ (a), $3a_1$ (b), $1b_2$ (c), and $2a_1$ (d), using ONIOM embedding. Average distance of the oxygen atoms (O, blue), average distance of the hydrogen atoms (H, orange), distance of the oxygen involved in the formation of the OH radical (OH, green), and distance of the excess proton (p, red). The error bars depict the standard error. The shaded red areas depict the standard deviation for the proton. The dotted lines show the maximum oxygen (blue) and hydrogen (orange) distances in the QM region.

the excess proton. Remarkably, the bias is much less for the inner-valence hole: Here, the average COM distance of OH matches the one for O.

The same analysis is shown in Fig. 11 for the ONIOM embedding. Overall, very similar curves can be seen for the average distances of O, H, p, and OH from the COM. However, a clear temporal kink in the distance of OH from the COM is observed. It turns out that after the proton transfer has happened, the OH radical is being pushed out of the QM region, a behavior that is not observed for electrostatic embedding (Fig. 10), where the distances from the COM seem to remain rather constant. We thus consider this effect, which has been reported before in the supplementary material of Ref. 10, an artifact due to the specific interactions between the QM and MM regions neglected in the ONIOM embedding scheme. Apart from the two discussed differences (Figs. 8 and 9 and Figs. 11 and 10), we find that both embedding schemes give almost identical results for the proton transfer (see Appendix A).

IV. CONCLUSIONS

We have modeled the radiolysis of water after single ionization of various valence orbitals. Our calculations show that the ionization of outer-valence orbitals ($1b_1$, $3a_1$, and $1b_2$) leads to rapid internal conversion, eventual leading to ionized water in its ground state within tens of femtoseconds. The internal conversion mechanism is accompanied by a proton transfer reaction, where a proton of one water molecule is given to a neighboring water molecule. The time at which the proton transfer occurs depends on where the initial electron vacancy was created. For ionization from a $1b_1$ valence orbital, proton transfer occurs about 45 fs after the ionization, whereas for ionization from one of the deeper bound $3a_1$ and $1b_2$ orbitals, it takes about 70 and 90 fs, respectively.

For inner-valence vacancies in the $2a_1$ orbitals, internal conversion due to non-adiabatic couplings is much slower because of the energy gap between the inner-valence and outer-valence hole states. We observe that the proton transfer takes place 22 fs after ionization, which is considerably larger than the value reported for dimers.[27,28] We discuss the consequence of this result for the ICD decay in liquid water. Since proton transfer competes with the ICD channel, and measurements indicated that the efficiency for ICD in bulk water is larger than 50%,[28] our calculated time for proton transfer is consistent with the extrapolated ICD decay times computed for the dimer.[28]

The vibrational excitation energy created in the ionization is transported away within several hundred femtoseconds. If one considers an aqueous solution, the resulting rise in effective temperature might trigger further reactions involving solutes in the vicinity of the transiently hot region. This way, high-energy radiation could turn out to be a promising tool for prospective temperature-jump–pump–probe experiments for studying ultrafast chemical dynamics in aqueous solutions.

We have compared two different embedding schemes, ONIOM and electrostatic embedding, and find that the results, overall, are very similar. For ONIOM embedding, there is a trend that the OH radical is pushed out of the QM region, which is not the case for the electrostatic embedding. Moreover, the transport of vibrational energy seems to be somewhat faster with the electrostatic embedding compared to the ONIOM embedding.

ACKNOWLEDGMENTS
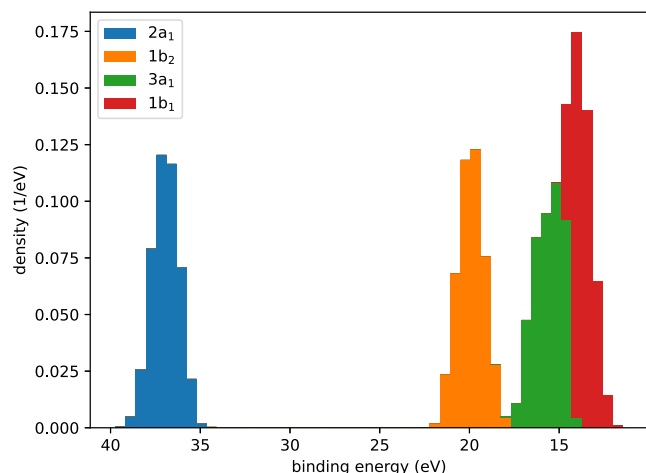
FIG. 12. Density of states obtained from the orbital energies of the sampled QM clusters.

AUTHOR DECLARATIONS

Conflict of Interest

The authors have no conflicts to disclose.

Author Contributions

Ludger Inhester: Conceptualization (lead); Formal analysis (equal); Software (equal); Visualization (equal); Writing – original draft (lead); Writing – review & editing (equal). **Arturo Sopena Moros**: Formal analysis (equal); Methodology (equal); Software (equal); Writing – review & editing (equal). **Sam Macé**: Formal analysis (equal); Visualization (equal); Writing – review & editing (equal). **Caroline Arnold**: Formal analysis (equal); Methodology (equal); Writing – review & editing (equal). **Robin Santra**: Conceptualization (supporting); Supervision (equal); Writing – review & editing (equal).

DATA AVAILABILITY

The data that support the findings of this study are available from the corresponding author upon reasonable request.

APPENDIX A: FURTHER RESULTS FOR ONIOM EMBEDDING

Here, we present further results for the ONIOM-embedding scheme analogous to those presented in the main text for the electrostatic-embedding scheme. Figure 12 shows the density of states obtained for the ONIOM embedding. It shows very similar distributions as those for the electrostatic embedding shown in Fig. 2.

The active-state populations for the ONIOM embedding are shown in Fig. 13 together with a fit to a kinetic-rate-equation model that assumes a decay $1b_2^{-1} \to 3a_1^{-1} \to 1b_1^{-1}$. Overall, we conclude that the differences to the electrostatic-embedding scheme are insignificant.
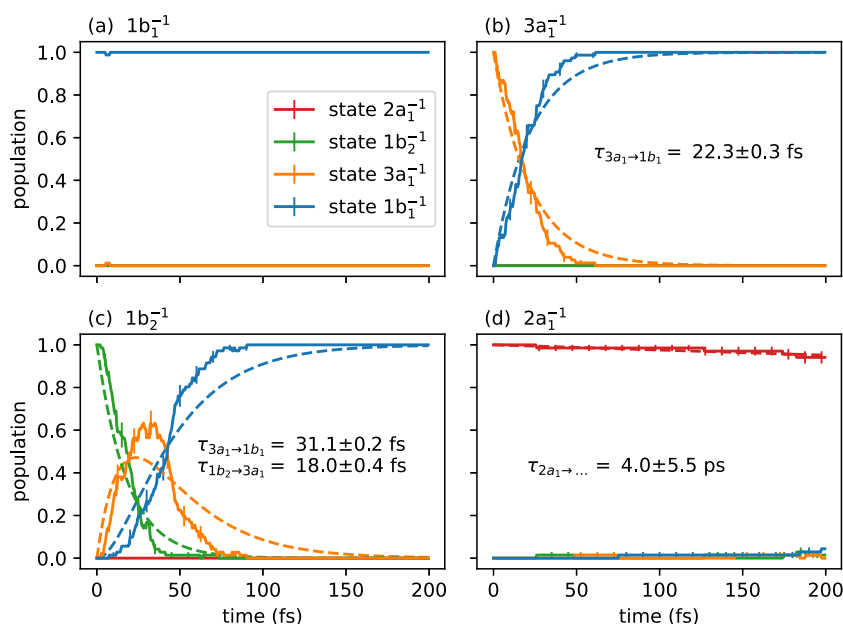
FIG. 13. Active-state populations for trajectories starting with an initial valence hole in $1b_1$ (a), $3a_1$ (b), $1b_2$ (c), and $2a_1$ (d), using ONIOM embedding. The error bars indicate the standard error. The dashed lines show fits to a rate equation model assuming a sequential decay $1b_2^{-1} \to 3a_1^{-1} \to 1b_1^{-1}$. For $2a_1$, only a single decay is fitted.

Figure 14 shows the average number of proton transfers giving very similar trends as for the electrostatic embedding shown in Fig. 5.

The evolution with respect to the proton-transfer coordinates obtained with the ONIOM-embedding scheme is shown in Fig. 15 in analogy to Fig. 6. Almost the same proton transfer times are obtained.

APPENDIX B: COMPARISON WITH RESULTS FOR A SMALLER QM REGION

The strong similarity of the results based on the two embedding strategies suggests that the electronic decay and the proton transfer are largely determined by the local environment around the ionized water molecule and less influenced by the chemical
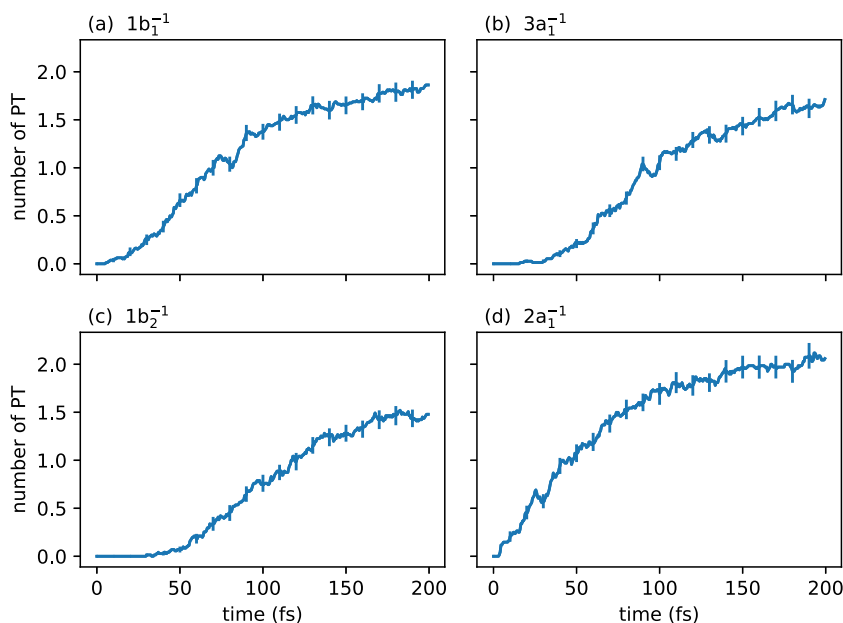

FIG. 14. Average number of proton transfers (PTs) as a function of time for trajectories starting with an initial valence hole in $1b_1$ (a), $3a_1$ (b), $1b_2$ (c), and $2a_1$ (d), using ONIOM embedding. The error bars indicate the standard error.

FIG. 15. Proton-transfer coordinates for trajectories starting with an initial valence hole in $1b_1$ (a), $3a_1$ (b), $1b_2$ (c), and $2a_1$ (d), using ONIOM embedding. The error bars indicate the standard error.
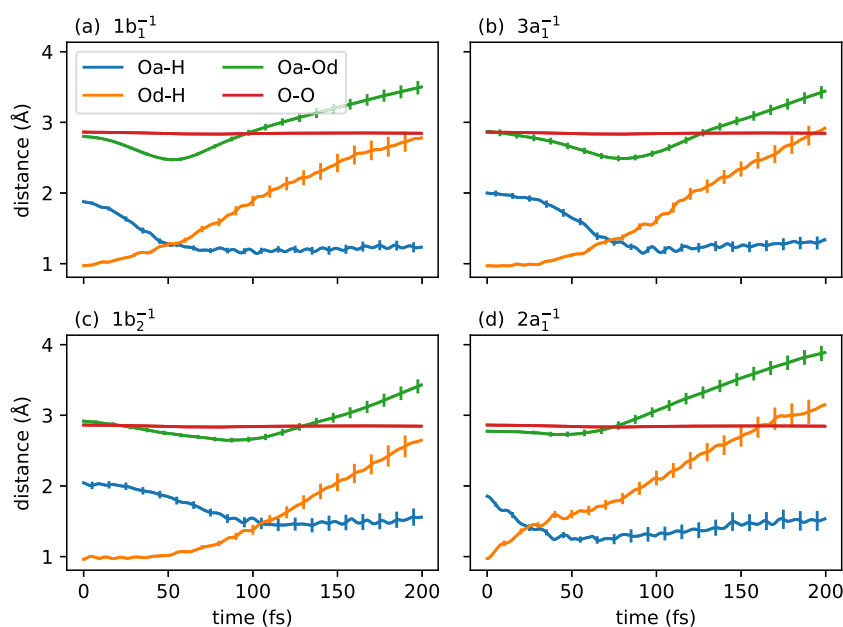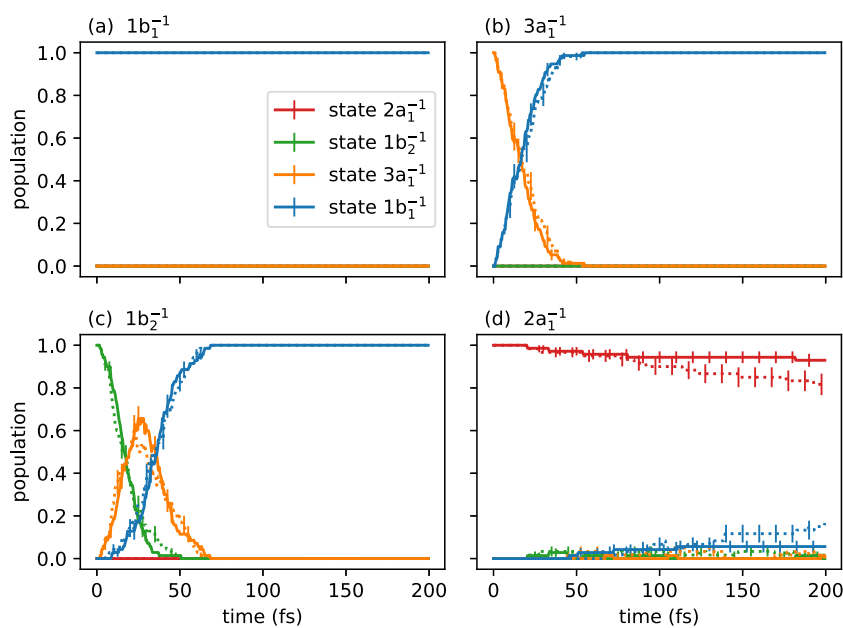
23 April 2025 08:13:16

FIG. 16. Active-state populations for trajectories starting with an initial valence hole in $1b_1$ (a), $3a_1$ (b), $1b_2$ (c), and $2a_1$ (d), using electrostatic embedding. Compared are results for QM regions with ten water molecules (dotted lines) and 12 water molecules (solid lines). The error bars indicate the standard error.

FIG. 17. Proton-transfer coordinates for trajectories starting with an initial valence hole in $1b_1$ (a), $3a_1$ (b), $1b_2$ (c), and $2a_1$ (d), using electrostatic embedding. Compared are results for QM regions with ten water molecules (dotted lines) and 12 water molecules (solid lines). The error bars indicate the standard error.
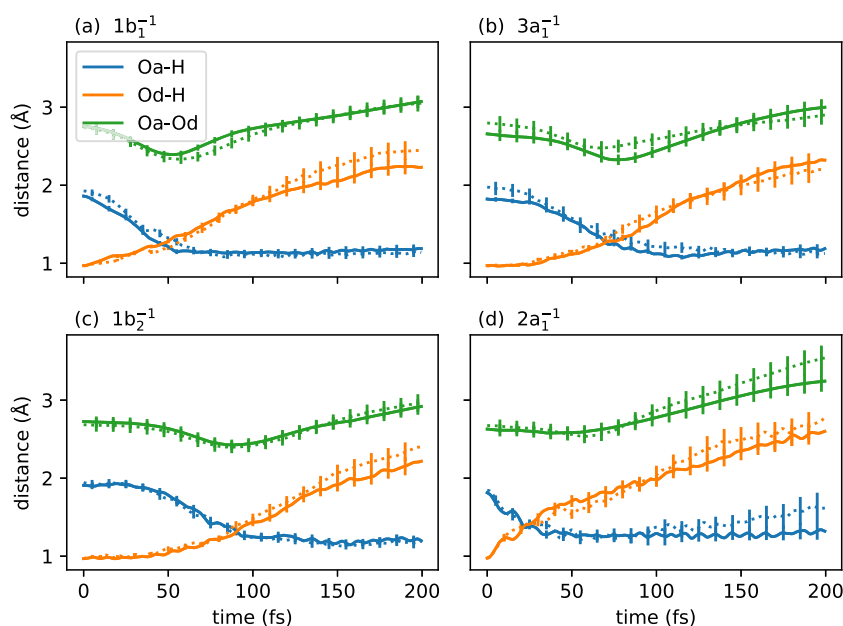
environment farther away. One can, therefore, expect that the results are converged already with a relatively small QM region. To test the convergence with respect to the size of the QM region, we performed additional simulations for a smaller QM region including only ten water molecules.

Figure 16 shows electronic state populations for both QM regions analogous to Fig. 4. One can see that the results are largely compatible within the respective error margins. The only exception is the somewhat faster decay for $2a_1^{-1}$ valence-hole states for the smaller QM region. As a further test, we compare the evolution

of the proton-transfer coordinate in Fig. 17. In addition, here, the results are largely the same within the error margins.

The compatibility of both results indicates that the results are largely converged with respect to the size of the QM region.

REFERENCES

[1]B. Boudaïffa, P. Cloutier, D. Hunting, M. A. Huels, and L. Sanche, "Resonant formation of DNA strand breaks by low-energy (3 to 20 eV) electrons," Science **287**, 1658–1660 (2000).

[2]M. Baumann, M. Krause, J. Overgaard, J. Debus, S. M. Bentzen, J. Daartz, C. Richter, D. Zips, and T. Bortfeld, "Radiation oncology in the era of precision medicine," Nat. Rev. Cancer **16**, 234–249 (2016).

[3]B. C. Garrett, D. A. Dixon, D. M. Camaioni, D. M. Chipman, M. A. Johnson, C. D. Jonah, G. A. Kimmel, J. H. Miller, T. N. Rescigno, P. J. Rossky, S. S. Xantheas, S. D. Colson, A. H. Laufer, D. Ray, P. F. Barbara, D. M. Bartels, K. H. Becker, K. H. Bowen, Jr., S. E. Bradforth, I. Carmichael, J. V. Coe, L. R. Corrales, J. P. Cowin, M. Dupuis, K. B. Eisenthal, J. A. Franz, M. S. Gutowski, K. D. Jordan, B. D. Kay, J. A. LaVerne, S. V. Lymar, T. E. Madey, C. W. McCurdy, D. Meisel, S. Mukamel, A. R. Nilsson, T. M. Orlando, N. G. Petrik, S. M. Pimblott, J. R. Rustad, G. K. Schenter, S. J. Singer, A. Tokmakoff, L.-S. Wang, and T. S. Zwier, "Role of water in electron-initiated processes and radical chemistry: Issues and scientific advances," Chem. Rev. **105**, 355–390 (2005).

[4]C. F. Perry, P. Zhang, F. B. Nunes, I. Jordan, A. von Conta, and H. J. Wörner, "Ionization energy of liquid water revisited," J. Phys. Chem. Lett. **11**, 1789–1794 (2020).

[5]S. Dey, S. D. Folkestad, A. C. Paul, H. Koch, and A. I. Krylov, "Core-ionization spectrum of liquid water," Phys. Chem. Chem. Phys. **26**, 1845–1859 (2024).

[6]S. Thürmer, M. Ončák, N. Ottosson, R. Seidel, U. Hergenhahn, S. E. Bradforth, P. Slavíček, and B. Winter, "On the nature and origin of dicationic, charge-separated species formed in liquid water on X-ray irradiation," Nat. Chem. **5**, 590–596 (2013).

[7]P. Slavíček, B. Winter, L. S. Cederbaum, and N. V. Kryzhevoi, "Proton-transfer mediated enhancement of nonlocal electronic relaxation processes in X-ray irradiated liquid water," J. Am. Chem. Soc. **136**, 18170–18176 (2014).

[8]T. Jahnke, R. Guillemin, L. Inhester, S.-K. Son, G. Kastirke, M. Ilchen, J. Rist, D. Trabert, N. Melzer, N. Anders, T. Mazza, R. Boll, A. De Fanis, V. Music, Th. Weber, M. Weller, S. Eckart, K. Fehre, S. Grundmann, A. Hartung, M. Hofmann, C. Janke, M. Kircher, G. Nalin, A. Pier, J. Siebert, N. Strenger, I. Vela-Perez, T. M. Baumann, P. Grychtol, J. Montano, Y. Ovcharenko, N. Rennhack, D. E. Rivas, R. Wagner, P. Ziolkowski, P. Schmidt, T. Marchenko, O. Travnikova, L. Journel, I. Ismail, E. Kukk, J. Niskanen, F. Trinter, C. Vozzi, M. Devetta, S. Stagira, M. Gisselbrecht, A. L. Jäger, X. Li, Y. Malakar, M. Martins, R. Feifel, L. Ph. H. Schmidt, A. Czasch, G. Sansone, D. Rolles, A. Rudenko, R. Moshammer, R. Dörner, M. Meyer, T. Pfeifer, M. S. Schöffler, R. Santra, M. Simon, and M. N. Piancastelli, "Inner-shell-ionization-induced femtosecond structural dynamics of water molecules imaged at an X-ray free-electron laser," Phys. Rev. X **11**, 041044 (2021).

[9]O. Marsalek, C. G. Elles, P. A. Pieniazek, E. Pluhařová, J. VandeVondele, S. E. Bradforth, and P. Jungwirth, "Chasing charge localization and chemical reactivity following photoionization in liquid water," J. Chem. Phys. **135**, 224510 (2011).

[10]Z.-H. Loh, G. Doumy, C. Arnold, L. Kjellsson, S. H. Southworth, A. Al Haddad, Y. Kumagai, M.-F. Tu, P. J. Ho, A. M. March, R. D. Schaller, M. S. Bin Mohd Yusof, T. Debnath, M. Simon, R. Welsch, L. Inhester, K. Khalili, K. Nanda, A. I. Krylov, S. Moeller, G. Coslovich, J. Koralek, M. P. Minitti, W. F. Schlotter, J.-E. Rubensson, R. Santra, and L. Young, "Observation of the fastest chemical processes in the radiolysis of water," Science **367**, 179–182 (2020).

[11]S. Li, L. Lu, S. Bhattacharyya, C. Pearce, K. Li, E. T. Nienhuis, G. Doumy, R. D. Schaller, S. Moeller, M.-F. Lin, G. Dakovski, D. J. Hoffman, D. Garratt, K. A. Larsen, J. D. Koralek, C. Y. Hampton, D. Cesar, J. Duris, Z. Zhang, N. Sudar, J. P. Cryan, A. Marinelli, X. Li, L. Inhester, R. Santra, and L. Young, "Attosecond-pump attosecond-probe x-ray spectroscopy of liquid water," Science **383**, 1118–1122 (2024).

[12]V. Svoboda, R. Michiels, A. C. LaForge, J. Med, F. Stienkemeier, P. Slavíček, and H. J. Wörner, "Real-time observation of water radiolysis and hydrated electron formation induced by extreme-ultraviolet pulses," Sci. Adv. **6**, eaaz0385 (2020).

[13]L. Lu, A. Wildman, A. J. Jenkins, L. Young, A. E. Clark, and X. Li, "The 'hole' story in ionized water from the perspective of Ehrenfest dynamics," J. Phys. Chem. Lett. **11**, 9946–9951 (2020).

[14]M.-F. Lin, N. Singh, S. Liang, M. Mo, J. P. F. Nunes, K. Ledbetter, J. Yang, M. Kozina, S. Weathersby, X. Shen, A. A. Cordones, T. J. A. Wolf, C. D. Pemmaraju, M. Ihme, and X. J. Wang, "Imaging the short-lived hydroxyl-hydronium pair in ionized liquid water," Science **374**, 92–95 (2021).

[15]O. Svoboda, D. Hollas, M. Ončák, and P. Slavíček, "Reaction selectivity in an ionized water dimer: Nonadiabatic *ab initio* dynamics simulations," Phys. Chem. Chem. Phys. **15**, 11531–11542 (2013).

[16]K. Schnorr, M. Belina, S. Augustin, H. Lindenblatt, Y. Liu, S. Meister, T. Pfeifer, G. Schmid, R. Treusch, F. Trost, P. Slavíček, and R. Moshammer, "Direct tracking of ultrafast proton transfer in water dimers," Sci. Adv. **9**, eadg7864 (2023).

[17]L. S. Cederbaum, J. Zobeley, and F. Tarantelli, "Giant intermolecular decay and fragmentation of clusters," Phys. Rev. Lett. **79**, 4778–4781 (1997).

[18]R. Santra, J. Zobeley, L. S. Cederbaum, and N. Moiseyev, "Interatomic Coulombic decay in van der Waals clusters and impact of nuclear motion," Phys. Rev. Lett. **85**, 4490–4493 (2000).

[19]S. Marburger, O. Kugeler, U. Hergenhahn, and T. Möller, "Experimental evidence for interatomic Coulombic decay in Ne clusters," Phys. Rev. Lett. **90**, 203401 (2003).

[20]T. Jahnke, A. Czasch, M. S. Schöffler, S. Schössler, A. Knapp, M. Käsz, J. Titze, C. Wimmer, K. Kreidi, R. E. Grisenti, A. Staudte, O. Jagutzki, U. Hergenhahn, H. Schmidt-Böcking, and R. Dörner, "Experimental observation of interatomic Coulombic decay in neon dimers," Phys. Rev. Lett. **93**, 163401 (2004).

[21]T. Jahnke, "Interatomic and intermolecular Coulombic decay: The coming of age story," J. Phys. B: At., Mol. Opt. Phys. **48**, 082001 (2015).

[22]T. Jahnke, U. Hergenhahn, B. Winter, R. Dörner, U. Frühling, P. V. Demekhin, K. Gokhberg, L. S. Cederbaum, A. Ehresmann, A. Knie, and A. Dreuw, "Interatomic and intermolecular Coulombic decay," Chem. Rev. **120**, 11295–11369 (2020).

[23]T. Jahnke, H. Sann, T. Havermeier, K. Kreidi, C. Stuck, M. Meckel, M. Schöffler, N. Neumann, R. Wallauer, S. Voss, A. Czasch, O. Jagutzki, A. Malakzadeh, F. Afaneh, T. Weber, H. Schmidt-Böcking, and R. Dörner, "Ultrafast energy transfer between water molecules," Nat. Phys. **6**, 139–142 (2010).

[24]M. Mucke, M. Braune, S. Barth, M. Förstel, T. Lischke, V. Ulrich, T. Arion, U. Becker, A. Bradshaw, and U. Hergenhahn, "A hitherto unrecognized source of low-energy electrons in water," Nat. Phys. **6**, 143–146 (2010).

[25]S. D. Stoychev, A. I. Kuleff, and L. S. Cederbaum, "Intermolecular Coulombic decay in small biochemically relevant hydrogen-bonded systems," J. Am. Chem. Soc. **133**, 6817–6824 (2011).

[26]P. Zhang, C. Perry, T. T. Luu, D. Matselyukh, and H. J. Wörner, "Intermolecular Coulombic decay in liquid water," Phys. Rev. Lett. **128**, 133001 (2022).

[27]R. Kumar, A. Ghosh, and N. Vaval, "Relaxation of the $2a_1$ ionized water dimer: An interplay of intermolecular Coulombic decay (ICD) and proton transfer processes," J. Chem. Phys. **160**, 214302 (2024).

[28]C. Richter, D. Hollas, C.-M. Saak, M. Förstel, T. Miteva, M. Mucke, O. Björneholm, N. Sisourat, P. Slavíček, and U. Hergenhahn, "Competition between proton transfer and intermolecular Coulombic decay in water," Nat. Commun. **9**, 4988 (2018).

[29]G. Groenhof, "Introduction to QM/MM simulations," Methods Mol. Biol. **924**, 43–66 (2013).

[30]M. J. Abraham, T. Murtola, R. Schulz, S. Páll, J. C. Smith, B. Hess, and E. Lindahl, "GROMACS: High performance molecular simulations through multi-level parallelism from laptops to supercomputers," SoftwareX **1–2**, 19–25 (2015).

[31]H. J. C. Berendsen, J. R. Grigera, and T. P. Straatsma, "The missing term in effective pair potentials," J. Phys. Chem. **91**, 6269–6271 (1987).

[32]G. Bussi, D. Donadio, and M. Parrinello, "Canonical sampling through velocity rescaling," J. Chem. Phys. **126**, 014101 (2007).

[33]B. Hess, C. Kutzner, D. van der Spoel, and E. Lindahl, "GROMACS 4: Algorithms for highly efficient, load-balanced, and scalable molecular simulation," J. Chem. Theory Comput. **4**, 435–447 (2008).

[34]Y. Hao, L. Inhester, K. Hanasaki, S.-K. Son, and R. Santra, "Efficient electronic structure calculation for molecular ionization dynamics at high x-ray intensity," Struct. Dyn. **2**, 041707 (2015).

[35]L. Inhester, K. Hanasaki, Y. Hao, S.-K. Son, and R. Santra, "X-ray multiphoton ionization dynamics of a water molecule irradiated by an x-ray free-electron laser pulse," Phys. Rev. A **94**, 023422 (2016).

[36]T. Clark, J. Chandrasekhar, G. W. Spitznagel, and P. V. R. Schleyer, "Efficient diffuse function-augmented basis sets for anion calculations. III. The 3-21+G basis set for first-row elements, Li–F," J. Comput. Chem. **4**, 294–301 (1983).

[37]W. J. Hehre, R. Ditchfield, and J. A. Pople, "Self—Consistent molecular orbital methods. XII. Further extensions of Gaussian—Type basis sets for use in molecular orbital studies of organic molecules," J. Chem. Phys. **56**, 2257–2261 (1972).

23 April 2025 08:13:16

[38] M. Svensson, S. Humbel, R. D. J. Froese, T. Matsubara, S. Sieber, and K. Morokuma, "ONIOM: A multilayered integrated MO + MM method for geometry optimizations and single point energy predictions. A test for Diels–Alder reactions and Pt(P(t-Bu)$_3$)$_2$ + H$_2$ oxidative addition," J. Phys. Chem. **100**, 19357–19363 (1996).

[39] L. Inhester, Z. Jurek, S.-K. Son, R. Santra, and A. Malik Muhammad, XRAYPAC, Zenodo, 2023.

[40] Q. Sun, "The updates in Libcint 6: More integrals, API refinements, and SIMD optimization techniques," J. Chem. Phys. **160**, 174116 (2024).

[41] Z. Li, M. El-Amine Madjet, O. Vendrell, and R. Santra, "Core-level transient absorption spectroscopy as a probe of electron hole relaxation in photoionized H$^+$(H$_2$O)$_n$," Faraday Discuss. **171**, 457–470 (2014).

[42] K. Khalili, L. Inhester, C. Arnold, R. Welsch, J. W. Andreasen, and R. Santra, "Hole dynamics in a photovoltaic donor-acceptor couple revealed by simulated time-resolved X-ray absorption spectroscopy," Struct. Dyn. **6**, 044102 (2019).

[43] Y. Shakya, L. Inhester, C. Arnold, R. Welsch, and R. Santra, "Ultrafast time-resolved x-ray absorption spectroscopy of ionized urea and its dimer through *ab initio* nonadiabatic dynamics," Struct. Dyn. **8**, 034102 (2021).

[44] Z. Yin, Y.-P. Chang, T. Balčiūnas, Y. Shakya, A. Djorović, G. Gaulier, G. Fazio, R. Santra, L. Inhester, J.-P. Wolf, and H. J. Wörner, "Femtosecond proton transfer in urea solutions probed by X-ray spectroscopy," Nature **619**, 749–754 (2023).

[45] A. T. B. Gilbert, N. A. Besley, and P. M. W. Gill, "Self-consistent field calculations of excited states using the maximum overlap method (MOM)," J. Phys. Chem. A **112**, 13164–13171 (2008).

[46] G. M. J. Barca, A. T. B. Gilbert, and P. M. W. Gill, "Simple models for difficult electronic excitations," J. Chem. Theory Comput. **14**, 1501–1509 (2018).

[47] B. Cordero, V. Gómez, A. E. Platero-Prats, M. Revés, J. Echeverría, E. Cremades, F. Barragán, and S. Alvarez, "Covalent radii revisited," Dalton Trans. **2008**, 2832–2838.

[48] J. Gerratt and I. M. Mills, "Force constants and dipole-moment derivatives of molecules from perturbed Hartree–Fock calculations. I," J. Chem. Phys. **49**, 1719–1729 (1968).

[49] J. A. Pople, R. Krishnan, H. B. Schlegel, and J. S. Binkley, "Derivative studies in Hartree–Fock and Møller–Plesset theories," Int. J. Quantum Chem. **16**, 225–241 (1979).

[50] Q. Cui and M. Karplus, "Molecular properties from combined QM/MM methods. I. Analytical second derivative and vibrational calculations," J. Chem. Phys. **112**, 1133–1149 (2000).

[51] C. F. Perry, I. Jordan, P. Zhang, A. von Conta, F. B. Nunes, and H. J. Wörner, "Photoelectron spectroscopy of liquid water with tunable extreme-ultraviolet radiation: Effects of electron scattering," J. Phys. Chem. Lett. **12**, 2990–2996 (2021).

[52] C. J. T. De Grotthuss, "Sur la décomposition de l'eau et des corps qu'elle tient en dissolution à l'aide de l'électricité galvanique," Ann. Chim. **58**, 54 (1806).

[53] D. Marx, "Proton transfer 200 years after von Grotthuss: Insights from ab initio simulations," ChemPhysChem **7**, 1848–1870 (2006).

[54] J. E. Crooks, "The temperature-jump technique for the study of fast reactions in solution," J. Phys. E: Sci. Instrum. **16**, 1142 (1983).

[55] P. K. Mishra, O. Vendrell, and R. Santra, "Ultrafast energy transfer from solvent to solute induced by subpicosecond highly intense THz pulses," J. Phys. Chem. B **119**, 8080–8086 (2015).

[56] C. Arnold, L. Inhester, S. Carbajo, R. Welsch, and R. Santra, "Simulated XUV photoelectron spectra of THz-pumped liquid water," J. Chem. Phys. **150**, 044505 (2019).

[57] N. Chakrabarti, E. Tajkhorshid, B. Roux, and R. Pomès, "Molecular basis of proton blockage in aquaporins," Structure **12**, 65–74 (2004).

23 April 2025 08:13:16